NJC

ROYAL SOCIETY OF CHEMISTRY

PAPER

View Article Online
View Journal

Cite this: DOI: 10.1039/d1nj04816c

Newly synthesized series of oxoindole–oxadiazole conjugates as potential anti-SARS-CoV-2 agents: *in silico* and *in vitro* studies†

Rana M. El-Masry,[a] Ahmed A. Al-Karmalawy,*[b] Radwan Alnajjar,[cd] Sara H. Mahmoud,[e] Ahmed Mostafa,[e] Hanan H. Kadry,[f] Sahar M. Abou-Seri*[g] and Azza T. Taher*[fh]

In this study, a series of 1,3,4-oxadiazoles carrying the isatin moiety (**IV$_{a-g}$**) as anti-SARS-CoV-2 agents were designed and synthesized. Molecular docking of the compounds (**IV$_{a-g}$**) into the SARS-CoV-2 M^{pro} active site showed promising binding affinities. The docking results were supported using molecular dynamics simulations and MM-GBSA calculations as well. To validate the *in silico* predictions, all compounds were evaluated for their half-maximal cytotoxicity (CC_{50}) and virus-inhibitory (IC_{50}) concentrations. The CC_{50} concentrations were remarkably high for most of the tested compounds. However, compounds **IV$_e$** and **IV$_g$** showed high activity against SARS-CoV-2 at IC_{50} values of 13.84 μM and 4.63 μM, with selectivity indices of 4.1 and 5.9, respectively. The most potent antiviral agent **IV$_g$** demonstrated an IC_{50} of 16.6 μM against SARS-CoV-2 M^{pro}, which is considered a moderate activity. However, the represented cellular antiviral activity of **IV$_g$** could justify further optimization to develop this series of compounds as broad-spectrum anti-SARS-CoV-2 agents.

Received 8th October 2021,
Accepted 4th February 2022

DOI: 10.1039/d1nj04816c

rsc.li/njc

1. Introduction

In December 2019, a cluster of infectious pneumonia cases was caused by a novel coronavirus that was reported in Wuhan, China.[1,2] Genomic sequencing revealed that this pathogenic coronavirus is 96% identical to a bat coronavirus and shares 79.6% sequence identity to SARS-CoV.[3–5] This novel coronavirus was named severe acute respiratory syndrome coronavirus 2 (SARS-CoV-2) by the International Committee on Taxonomy of Viruses. The resulting pneumonia was designated as coronavirus disease 2019 (COVID-19) by the World Health Organization (WHO) on February 11, 2020.[6] The WHO recognized COVID-19 as a global threat as it rapidly spreads and broke out in more than 212 countries, causing significant health and economic impacts.[7,8]

SARS-CoV-2 is characterized by four structural proteins: spike (S), envelope (E), membrane (M), and nucleocapsid (N). The spike protein enables binding of SARS-COV-2 to the angiotensin-converting enzyme-2 (ACE-2), which is expressed on the surface of several pulmonary and extra-pulmonary cells causing the spread of the infection to many types of host cells.[9] The viral genome also encodes non-structural proteins including papain-like protease (PL^{pro}), 3-chymotrypsin-like protease (3CL^{pro}), helicase, and RNA-dependent RNA polymerase (RdRp), which are the enzymes responsible for viral replication and transcription.[10] 3CL^{pro}, also known as the main protease (M^{pro}), is the key enzyme that plays an essential role in viral replication,[11] and has no homolog in human proteases.[12]

ACE-2 and M^{pro} are the main targets for drug development against SARS-COV-2. The active site of M^{pro} contains Cys145 and His41 in order to constitute a catalytic dyad, where cysteine functions as the common nucleophile in the proteolytic process.[13] Structures of the main proteases in different coronavirus strains show a remarkable degree of conservation on the substrate-binding sites. Thus, they have been considered an

[a] Organic Chemistry Department, Faculty of Pharmacy, October University for Modern Sciences and Arts (MSA), October 6 city, Giza, Egypt
[b] Department of Pharmaceutical Medicinal Chemistry, Faculty of Pharmacy, Horus University-Egypt, New Damietta 34518, Egypt. E-mail: akarmalawy@horus.edu.eg
[c] Department of Chemistry, Faculty of Science, University of Benghazi, Benghazi, Libya
[d] Department of Chemistry, University of Cape Town, Rondebosch 7701, South Africa
[e] Center of Scientific Excellence for Influenza Viruses, National Research Centre (NRC), Dokki, Giza 12622, Egypt
[f] Department of Pharmaceutical Organic Chemistry, Faculty of Pharmacy, Cairo University, Cairo, Egypt. E-mail: azza.shalaby@pharma.cu.edu.eg
[g] Department of Pharmaceutical Chemistry, Faculty of Pharmacy, Cairo University, Cairo, Egypt. E-mail: sahar.shaarawy@pharma.cu.edu.eg
[h] Department of Organic Pharmaceutical Chemistry, Faculty of Pharmacy, October 6 University (O6U), October 6 City, Giza, Egypt

† Electronic supplementary information (ESI) available. See DOI: 10.1039/d1nj04816c

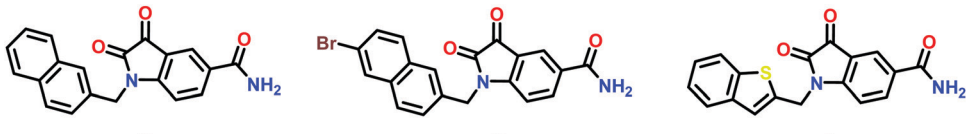

I_a IC_{50}= 45 nM I_b IC_{50}= 47 nM I_c IC_{50}= 53 nM

Fig. 1 Reported *N*-substituted isatin compounds showing inhibitory effect against SARS-CoV-2 M^{pro}.

attractive drug target and a structural basis for the rational drug design of anti-coronavirus therapy.[14,15]

Different drug-discovery approaches have been recently adopted to find several potential SARS-CoV-2 M^{pro} inhibitors, including compound library screening,[15–19] rational design,[1,15,20,21] and the testing of traditional Chinese medicine ingredients.[22–25] The chemical structures of the experimentally identified SARS-CoV-2 M^{pro} inhibitors are diverse, including α-ketoamide analogs,[20] peptidomimetic compounds,[1,15] baicalein and its derivatives,[22] and several repurposed approved drugs and drug candidates.[15] However, only a few drugs have high inhibitory activity against SARS-CoV-2 M^{pro}, and no clinically effective drug has been developed for the prevention or treatment of COVID-19. Therefore, specific anti-SARS-CoV-2 drugs, that offer efficacy and safety, are urgently needed.

Liu *et al.* synthesized a series of *N*-substituted isatin compounds, tested their inhibitory effects against SARS-CoV-2 M^{pro}, and studied their binding mode *via* molecular docking (Fig. 1). Biological evaluation results showed three potent compounds $\mathbf{I_{a–c}}$ that inhibit SARS-CoV-2 M^{pro} with IC_{50} values of 45, 47, and 53 nM, respectively.[26] The study indicated that *N*-substituted isatin compounds have the potential to be developed as broad-spectrum anti-coronavirus drugs.

To examine the potential binding mode of these compounds, the complex model structure of the most active compound $\mathbf{I_a}$ and SARS-CoV-2 M^{pro} was built using an induced-fit docking procedure.[27,28] Compound $\mathbf{I_a}$ fitted perfectly into the substrate-binding pocket of the enzyme, making interactions with the most important active-site residues. The side-chain carbonyl groups of Asn142 and Glu166 were involved in H-bond interactions with the carboxamide group at C-5 of the ligand. The main-chain NH group of Cys145 established H bonds with oxygen atoms at C-2 and C-3 of the isatin moiety. The naphthyl ring fitted into the hydrophobic groove that is lined with Met49 and Met165 and the complex was stabilized *via* pi–pi stacking interactions with His41.[26] There were three main pharmacophoric features that were considered to be essential for binding of the potent inhibitor $\mathbf{I_a}$ to the active site of SARS-CoV-2 M^{pro}: an H-bond donor to Glu166, an H-bond acceptor to interact with Cys145, and a lipophilic moiety to fit into the hydrophobic groove formed by Met49 and Met165.

Moreover, a previous computational screening study performed on 118 compounds with different heterocyclic moieties found that derivatives of isatin linked with oxadiazoles achieved the best docking scores and showed promise as potential inhibitors of M^{pro} for SARS-CoV-2.[12]

According to these results, and in continuation of our previous research targeting SARS-CoV-2,[4,5,16–19,21,23–25,29–38] a series of isatin Schiff bases that maintain these essential pharmacophoric features have been designed and synthesized, and their potential binding modes with the SARS-CoV-2 M^{pro} active site were examined. The free NH of isatin had the potential to act as an H-bond donor to Glu166, and the oxygen at C-2 of isatin served as an H-bond acceptor from His163 or Cys145. The arylisoxazole projected into the hydrophobic groove to interact with Met49 and Met165 as depicted in Fig. 2.

One of the most important and recent approaches to investigate the activity of a drug is computer-aided drug design (CADD).[39–49] In this study, the interaction between the designed compounds and the binding site was predicted using molecular docking to calculate the binding affinities.[50] Moreover, to confirm the results of molecular docking, molecular dynamics (MD) simulations for 100 ns were carried out on the best-docked inhibitor–protein complexes. This led to gaining further insight into the affinity between the ligands and the SARS-CoV-2 M^{pro} active site as well as evaluating the stability of the ligands within the binding site of the protein. These ligand–protein complexes were subjected to the molecular mechanics-generalized Born and surface area (MM-GBSA) calculations to evaluate the consistent relative binding free energies.

2. Results and discussion

2.1. Chemistry

The synthetic protocol for obtaining the target compounds 3-((5-aryl-1,3,4-oxadiazol-2-yl)imino)indolin-2-one $\mathbf{IV_{a–g}}$ is outlined in Scheme 1. The 5-substituted 1,3,4-oxadiazol-2-amine compounds $\mathbf{II_{a–c}}$ were prepared according to the reported method.[51] Refluxing compounds $\mathbf{II_{a–c}}$ with isatin derivatives $\mathbf{III_{a–c}}$ in acetic acid resulted in our title compounds $\mathbf{IV_{a–g}}$ in yields of 17–43%.

The structures of the achieved compounds $\mathbf{IV_{a–g}}$ were characterized through spectroscopic (IR, ^{1}H NMR, ^{13}C NMR, mass) as well as elemental analyses. Taking compound $\mathbf{IV_c}$ as an example, its IR spectrum is characterized by the presence of NH and C=O stretching bands at 3169 and 1671 cm^{-1}, respectively. The structure was also confirmed *via* its ^{1}H NMR spectrum, which showed a singlet signal at δ 3.87 ppm, assigned to the methoxy protons, and the appearance of two exchangeable singlet signals corresponding to the NH and OH protons of the tautomeric amide moiety at δ 11.37 and δ 13.90 ppm, respectively. Moreover, the aromatic protons of the oxoindole and the methoxyphenyl moieties were detected at δ 6.96–7.89 ppm with the expected multiplicity and integration. The ^{13}C NMR spectrum of target compound $\mathbf{IV_c}$ confirmed the

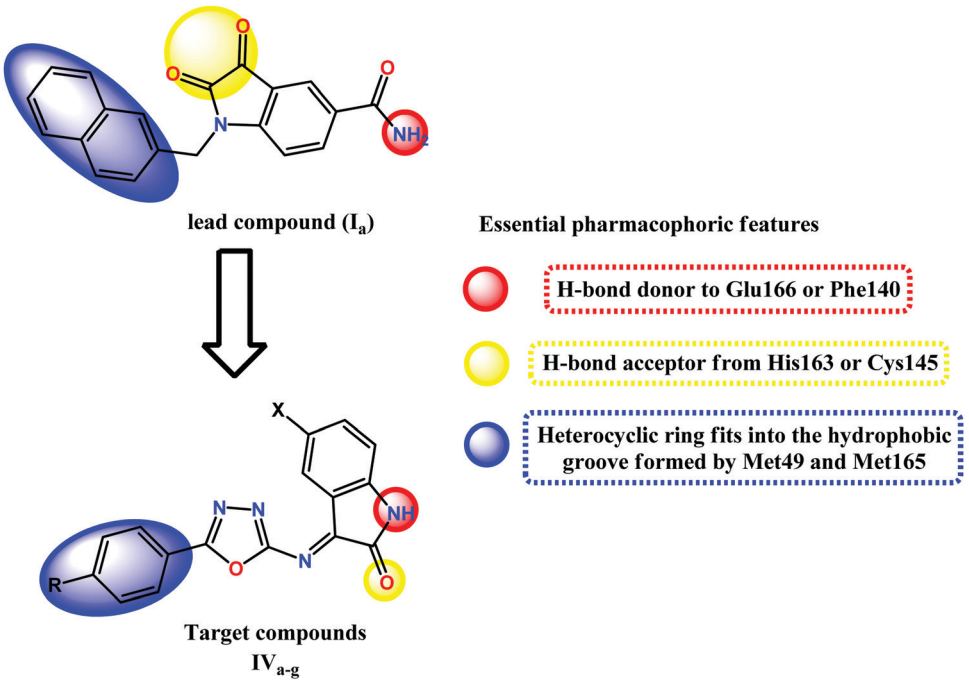

Fig. 2 Pharmacophoric features of the newly synthesized series of 1,3,4-oxadiazole–oxoindole conjugates (IV_{a-g}) based on the reported M^{pro} inhibitor (I_a).

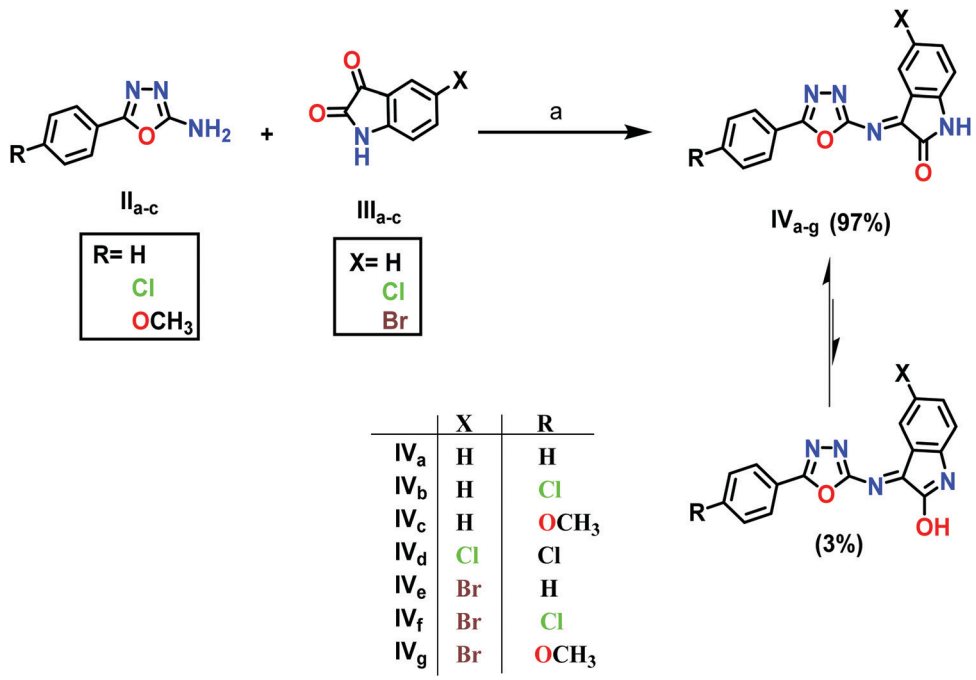

	X	R
IV_a	H	H
IV_b	H	Cl
IV_c	H	OCH_3
IV_d	Cl	Cl
IV_e	Br	H
IV_f	Br	Cl
IV_g	Br	OCH_3

Scheme 1 Synthesis of target compounds IV_{a-g}. *Reagents and conditions*: (a) acetic acid, reflux 38–50 h, yield = 17–43%.

presence of the C=O group of the oxoindole moiety *via* a signal at δ 163.32 ppm.

2.2. Biological evaluation results

2.2.1. Assessment of *in vitro* antiviral activity, cytotoxicity, and selectivity. The cytotoxicity and the virus-inhibitory effect of the synthesized compounds IV_{a-g} were tested by determining the half-maximal cytotoxic (CC_{50}) and inhibitory (IC_{50}) concentrations for each compound. The ratio of CC_{50} to IC_{50} was used to determine the selectivity index for each compound. Except for IV_b and IV_d, which displayed minor cytotoxicity, the CC_{50} concentrations were remarkably high for all tested compounds.

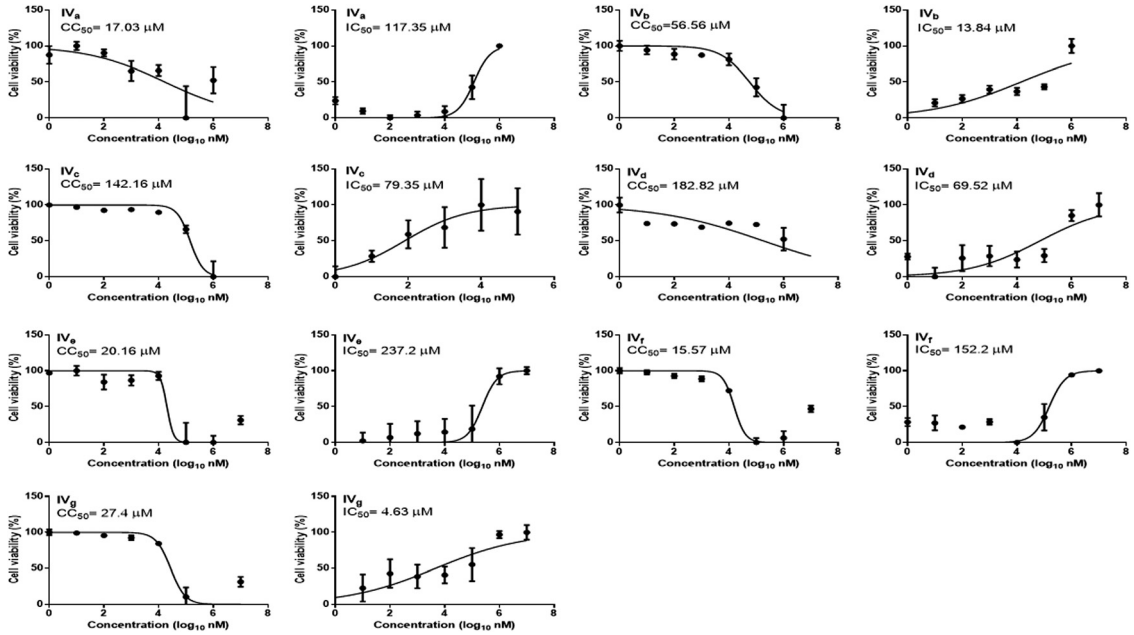

Fig. 3 Dose–response curves for the tested oxadiazole derivatives in Vero-E6 cells. Non-linear regression analysis using GraphPad Prism software (version 5.01) was carried out to calculate the CC_{50} and IC_{50} values by plotting log inhibitor *versus* normalized response (variable slope).

However, compounds **IV$_e$** and **IV$_g$** showed high antiviral activity against SARS-CoV-2 with IC_{50} values of 13.84 μM and 4.63 μM, and selectivity indices of 4.1 and 5.9, respectively (Fig. 3 and Table 1). On the other hand, compounds **IV$_b$** and **IV$_d$** showed low cytotoxic (142.16 and 182.82 μM) and inhibitory concentrations (79.35 and 69.52 μM), with selectivity indices of 1.8 and 2.6, respectively. Finally, compounds **IV$_a$**, **IV$_c$**, and **IV$_f$** did not induce any inhibition activity against SARS-CoV-2 at safe concentrations. Further optimization to reduce the cytotoxicity and to increase the cellular antiviral activity seems to be necessary to develop this series of compounds as broad-spectrum anti-coronavirus drugs. Given the lack of anti-SARS-CoV-2 activity of most FDA-approved protease inhibitors,[27] the antiretroviral drug, lopinavir, an M^{pro} inhibitor (which is used for the treatment of HIV and is considered to be an active drug for the treatment of COVID-19),[52] showed moderate antiviral activity against SARS-CoV-2 with an IC_{50} value of 5.73 μM and a selectivity index of at least 8.[28] Furthermore, the known potent M^{pro} inhibitor **N3** hemihydrate displayed an antiviral activity of 16.77 μM.[20] Compared with lopinavir and **N3** hemihydrate, we assumed that **IV$_g$** might be a candidate protease inhibitor for combatting SARS-CoV-2 replication.

Table 1 Cytotoxicity and virus-inhibitory effect of the newly synthesized oxoindole–oxadiazole derivatives (**IV$_{a-g}$**) against SARS-CoV-2[a]

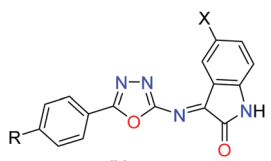

IV$_{a-g}$

Compound	X	R	CC_{50} (μM)	IC_{50} (μM)	Selectivity index, CC_{50}/IC_{50}
IV$_a$	H	H	17.03	117.35	0.15
IV$_b$	H	Cl	142.16	79.35	1.79
IV$_c$	H	OCH_3	15.57	152.2	0.10
IV$_d$	Cl	Cl	182.82	69.52	2.63
IV$_e$	Br	H	56.56	**13.84**	**4.08**
IV$_f$	Br	Cl	20.16	237.20	0.08
IV$_g$	Br	OCH_3	27.4	**4.63**	**5.92**

[a] Bold figures indicate high antiviral activity against SARS-CoV-2 IC50 < 20 μM and high selectivity SI > 3.

Regarding the SAR, the antiviral activity and selectivity of the synthesized oxoindole–oxadiazole conjugates seem to be affected by the C-5 substituent on the oxoindole ring. Except for compound **IV$_f$**, the introduction of the 5-Cl or 5-Br substituent to the oxoindole scaffold enhanced the antiviral potency and selectivity (compound **IV$_b$** ≠ **IV$_d$**, **IV$_a$** ≠ **IV$_e$** and **IV$_c$** ≠ **IV$_f$**). In particular, introducing the 5-bromo atom to the oxoindole ring in **IV$_c$** (IC_{50} = 152.20 μM, SI = 0.1) resulted in compound **IV$_f$** with about a 33- and a 59-fold increase in antiviral activity and selectivity, respectively.

A direct effect of *p*-substituent on the phenyloxadiazole moiety could not be observed. The introduction of an electron-withdrawing chloro substituent to the unsubstituted oxoindole derivative **IV$_a$** (IC_{50} = 117.35 μM, SI = 0.15) produced compound **IV$_b$** with a remarkable improvement in the antiviral activity and selectivity (IC_{50} = 79.35 μM, SI = 1.79). On the other hand, grafting an electron-donating *p*-methoxy group in compound **IV$_c$** reduced the antiviral activity and selectivity (IC_{50} = 152.20 μM, SI = 0.1). Attaching a *p*-Cl phenyloxadiazole moiety to the 5-bromo-oxoindole ring was detrimental to both the antiviral activity and the selectivity [compound **IV$_e$** (IC_{50} = 13.84 μM, SI = 4.08) ≠ compound **IV$_f$** (IC_{50} = 237.20 μM,

Table 2 Virus-inhibitory effect and M^{pro} inhibitory activity of the newly synthesized oxoindole–oxadiazole derivative ($\mathbf{IV_g}$) and reference compound **N3** against SARS-CoV-2

Compound	IC_{50} (μM)	
	Cell protection assay	M^{pro} enzyme inhibition
$\mathbf{IV_g}$	4.63	16.60
N3	16.77	0.40

SI = 0.08)], while substitution with the *p*-OCH_3 group produced the most potent and selective antiviral agent in this study, *i.e.*, $\mathbf{IV_g}$ (IC_{50} = 4.63 μM, SI = 5.92).

2.2.2. Assessment of *in vitro* SARS-CoV-2 main protease inhibitory activity. The cell protection assay results revealed that compound $\mathbf{IV_g}$ was the most active and selective compound of the newly synthesized series (IC_{50} = 4.63 μM, SI = 5.92). Comparing the antiviral activity of $\mathbf{IV_g}$ with the reported reference inhibitor **N3** hemihydrate (16.77 μM)[20] suggested that $\mathbf{IV_g}$ was a potent antiviral agent. According to the antiviral activity assay results, we opted to further evaluate compound $\mathbf{IV_g}$ for its inhibitory activity against SARS-CoV-2 M^{pro}. Surprisingly, compound $\mathbf{IV_g}$ demonstrated an IC_{50} of 16.60 μM against SARS-CoV-2 M^{pro}, which was considered as a moderate activity compared with the reported potent SARS-CoV-2 M^{pro} inhibitor **N3** hemihydrate (IC_{50} = 0.40 μM) (Table 2 and Fig. 4). As a result of the high cell protection activity of $\mathbf{IV_g}$ compared with **N3**, despite the moderate enzyme inhibition activity (Fig. 4), this compound was suggested to have an additional mode of action besides SARS-CoV-2 M^{pro} enzyme inhibition, which needs to be further investigated in the future.

In conclusion, compound $\mathbf{IV_g}$ was found to be an active inhibitor of SARS-CoV-2 M^{pro}, although it needs further optimization for better binding to the enzyme and better cellular activity for attaining lead compounds as broad-spectrum anti-COVID-19 drugs.

2.3. Molecular docking

The catalytic cleft between domains I and II of SARS-CoV-2 M^{pro} is composed of a Cys–His dyad where the inhibitor-binding site is located. The **N3** inhibitor is composed of only one polypeptide and is stabilized inside the binding pocket of SARS-CoV-2 M^{pro} showing an asymmetric unit.

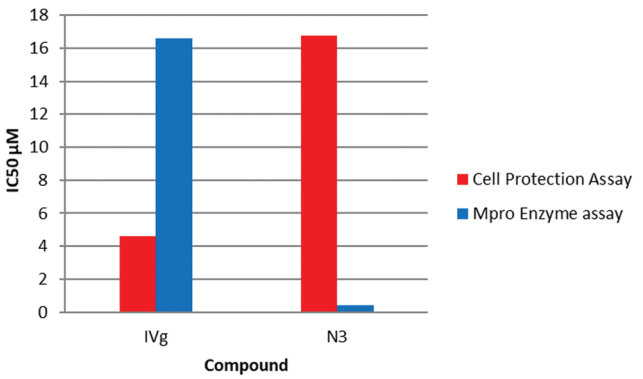

Fig. 4 Anti-viral and main protease inhibitory activities of compound $\mathbf{IV_g}$ and the reference inhibitor **N3** against SARS-CoV-2.

Table 3 Binding scores and interactions of the newly designed oxoindole–oxadiazole derivatives ($\mathbf{IV_{a-g}}$), ($\mathbf{I_a}$), and **N3** inhibitor (docked) into the **N3** binding pocket of SARS-CoV-2 M^{pro}

No.	Compound	S^a (kcal mol^{-1})	RMSD_Refine[b]	Amino acid bond	Distance (Å)
1	$\mathbf{IV_a}$	−5.59	1.39	Phe140/H-donor	2.96
				His163/H-acceptor	3.10
				Met165/pi-H	3.60
2	$\mathbf{IV_b}$	−6.37	0.89	Phe140/H-donor	2.90
				His163/H-acceptor	3.20
				Met165/pi-H	3.56
3	$\mathbf{IV_c}$	−6.32	0.99	Glu166/H-donor	3.12
				His163/H-acceptor	3.23
4	$\mathbf{IV_d}$	−5.97	1.32	Glu166/H-donor	3.21
				His163/H-acceptor	2.91
				His164/H-donor	3.13
5	$\mathbf{IV_e}$	−6.05	1.94	Cys145/H-acceptor	3.04
				Ser144/H-acceptor	3.11
				Glu166/p-Hi	3.89
6	$\mathbf{IV_f}$	−6.14	1.68	Glu166/H-donor	3.18
				His163/H-acceptor	3.26
7	$\mathbf{IV_g}$	−6.44	1.89	Glu166/H-donor	3.09
				His163/H-acceptor	3.27
8	$\mathbf{I_a}$	−6.09	2.41	Glu166/H-donor	3.23
				His163/H-acceptor	2.98
				Met165/pi-H	3.44
				His41/H-pi	3.82
9	**N3**	−9.98	1.91	Gln189/H-donor	2.96
				Glu166/H-acceptor	3.02
				Met49/H-donor	3.55
				Gly143/pi-H	4.76

[a] *S*, the score of a compound at the binding site of the protein. [b] RMSD_Refine, the root-mean-squared-deviation (RMSD) between the predicted pose and the crystal structure.

Molecular docking simulations were performed on the newly designed oxadiazole derivatives carrying the oxoindole moiety ($\mathbf{IV_{a-g}}$), the most potent previously reported isatin ($\mathbf{I_a}$), and the neutral inhibitor **N3** into the M^{pro} active site, and the obtained results are reported in Table 3.

The docked inhibitor **N3** occupied the receptor pocket with a similar binding mode compared to the co-crystallized conformer. It recorded a binding score of −9.98 kcal mol^{-1} and an RMSD of 1.91 Å. It was stabilized inside the binding pocket through the formation of three H-bonds: one with Gln189 at 2.96 Å, the second one with Glu166 at 3.02 Å, and the third with Met49 at 3.55 Å. Moreover, it formed a pi-H bond with Gly143 at 4.76 Å (Fig. 5).

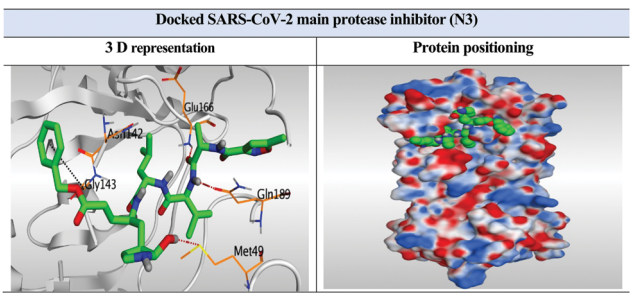

Fig. 5 3D representation and positioning for the docked **N3** inhibitor inside the SARS-CoV-2 M^{pro} pocket.

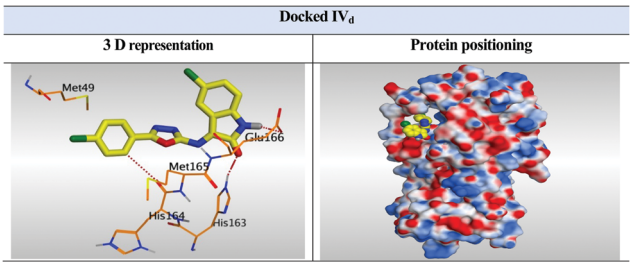

Fig. 6 3D representation and positioning of the docked **IV$_d$** inside the SARS-CoV-2 M^{pro} pocket.

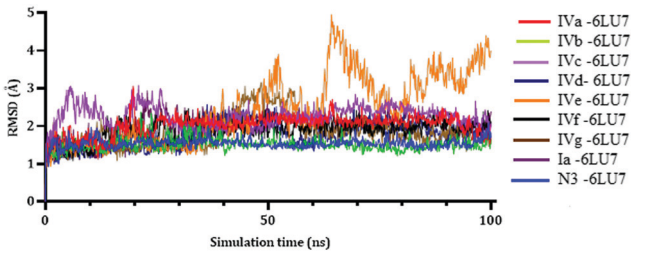

Fig. 8 Plots of RMSD for Cα atoms (Å) concerning the initial structure *vs.* the simulation time (ns) for all the complexes.

Interestingly, most of the newly designed oxadiazoles were found to form nearly the same binding mode compared to the previously reported isatin derivative (**I$_a$**) according to our aforementioned design rationale (Fig. 1).

As an example, compound **IV$_d$** was bound inside the SARS-CoV-2 main protease receptor pocket with a binding score of −5.97 kcal mol^{-1} and a 1.32 Å RMSD. As previously mentioned, the general binding mode of the synthesized oxadiazole derivatives was by fitting the enzyme pocket through the formation of two H-bonds with the most important Glu166 and His163 amino acids through the NH and carbonyl oxygen groups at 3.21 and 2.91 Å, respectively. Moreover, compound **IV$_d$** formed an extra H-bond with the His164 amino acid of the hydrophobic cleft at 3.13 Å. Also, the oxadiazole phenyl group fitted into the hydrophobic groove formed by Met49, Met165, and His164 (Fig. 6).

Besides the foregoing, compound **IV$_g$** fitted inside the large pocket with a binding score of (−6.44 kcal mol^{-1}) and a 1.89 Å RMSD. Also, it formed two hydrogen bonds with the two crucial amino acids (Glu166 and His163) through NH and carbonyl oxygen groups at 3.09 and 3.27 Å, respectively. Furthermore, the oxadiazole phenyl group fitted into the hydrophobic groove formed by Met49, Met165, and His164 (Fig. 7).

2.4. Molecular dynamics simulations

Protein and ligand RMSD analysis. To monitor the effect of the simulation on the conformational stability of 6LU7, RMSD values of the Cα atoms were estimated for all the complexes with respect to the initial structure. The results were plotted as a function of the simulation time in Fig. 8. As illustrated in Fig. 8, the protein was stable during simulation with an RMSD less than 3.00 Å except for the **IV$_e$–6LU7** complex where a protein backbone fluctuation started at around 40 ns and increased gradually. These fluctuations resulted from unfolded side chains (Fig. 5, ESI†), and no such fluctuations were exhibited by other complexes. On the other hand, **IV$_c$** and **IV$_f$** fluctuated till 30 ns before reaching equilibrium, while other complexes reached equilibrium at an early stage of the simulation.

The RMSD values of the ligands were plotted as a function of the simulation time to show the RMSD of a ligand that was aligned and measured just on its reference conformation within the active site. As shown in Fig. 9, compounds **IV$_a$**, **IV$_b$**, and **IV$_e$** moved by around 8 Å relative to their reference site before reaching equilibrium at 40 Å. On the other hand, **IV$_d$** and **IV$_f$** moved by around 5 Å from their original site till reaching equilibrium at 50 Å. Compounds **IV$_c$** and **IV$_g$** behaved differently: **IV$_c$** moved around 5 Å at the beginning of the simulation till 70 ns, then it moved a further 4 Å from its new site; **IV$_g$** was stable and moved only by 2 Å at 40 ns, and then moved a further 8 Å from its new position before reaching equilibrium. Finally, **I$_a$** fluctuated till 75 ns before reaching equilibrium in a new site, which was around 3 Å from its reference position.

As **IV$_d$** showed the strongest MM-GBSA (Table 4) binding energy, it was further investigated to get a better understanding of its interactions within the active site of the SARS-CoV-2 M^{pro}. As noticed in Fig. 10, **IV$_d$** was able to form an H-bond with the negatively charged amino acid glutamic Glu166 using the oxygen atom of the carbonyl group for 88% of the simulation time, and other weak H-bonding interactions were formed with Phe140, Asn142, Gly143, and Ser144 for less than 1% of the simulation time. Hydrophobic interactions were also formed, with a pi–pi interaction between the phenyl ring and the imidazole ring of His41, and another hydrophobic interaction

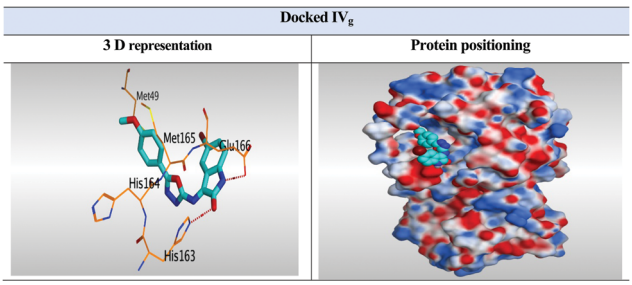

Fig. 7 3D representation and positioning of the docked **IV$_g$** inside the SARS-CoV-2 M^{pro} pocket.

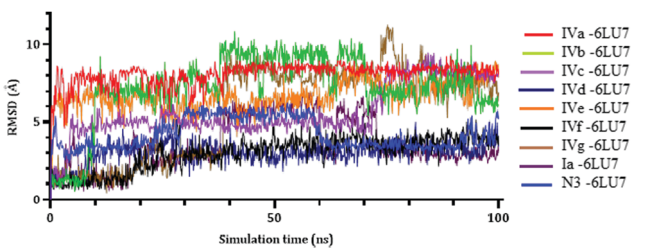

Fig. 9 Plots of RMSD data for ligand atoms (Å) concerning the initial structure *vs.* the simulation time (ns) for all the complexes.

Table 4 Prime MM-GBSA energies (in kcal mol^{-1}) for ligands binding at the active site of SARS-CoV-2 M^{pro}

Compound	ΔG binding	Coulomb	Covalent	H-bond	Bind packing	Lipo	Solv_GB	vdW
$\mathbf{IV_a}$	−46.56	−9.66	1.11	−0.79	−12.21	−1.75	14.25	−37.51
$\mathbf{IV_b}$	−37.61	−8.41	1.27	−0.75	−10.06	−1.01	14.79	−33.43
$\mathbf{IV_c}$	−51.66	−13.01	1.49	−0.91	−12.37	−3.69	18.07	−41.24
$\mathbf{IV_d}$	−54.98	−8.59	0.64	−0.76	−14.15	−5.87	17.21	−43.48
$\mathbf{IV_e}$	−48.18	−1.63	1.70	−0.12	−14.97	−1.12	10.82	−42.87
$\mathbf{IV_f}$	−48.03	−13.74	1.45	−0.98	−9.97	−4.88	20.31	−40.21
$\mathbf{IV_g}$	−49.82	−8.27	2.75	−1.02	−11.39	−3.01	16.13	−45.00
$\mathbf{I_a}$	−51.20	−17.68	2.41	−1.29	−11.68	−3.17	24.33	−44.12
N3	−71.47	−22.89	2.41	−1.75	−15.77	−0.87	33.16	−65.76

Coulomb, Coulomb energy; covalent, covalent binding energy; vdW, van der Waals energy; Lipo, lipophilic energy; Solv_GB, generalized Born electrostatic solvation energy; H-bond, hydrogen-bonding energy.

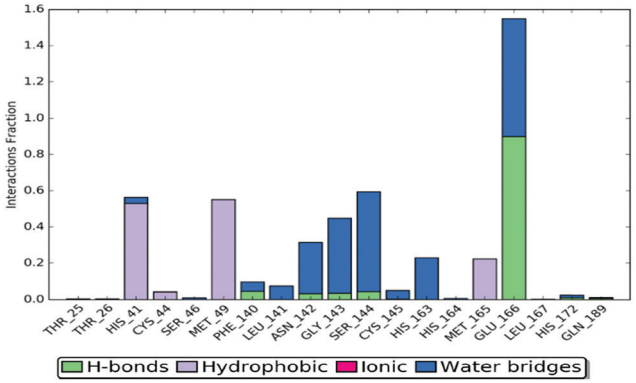

Fig. 10 Histogram of $\mathbf{IV_d}$–**6LU7** contact throughout the trajectory.

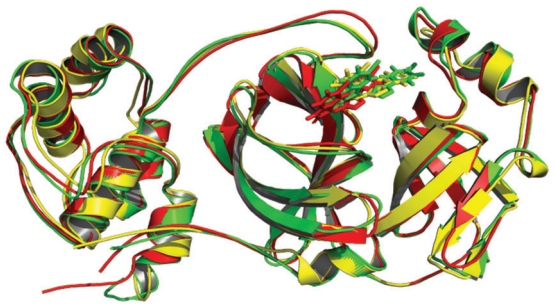

Fig. 11 Aligned structures of $\mathbf{IV_d}$–**6LU7** during simulations: red, 0 ns; yellow, 50 ns; green, 100 ns.

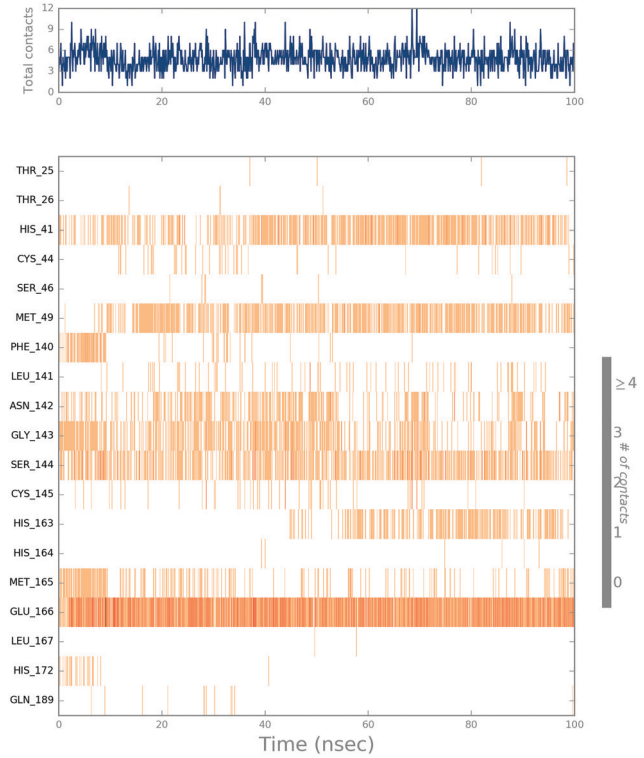

Fig. 12 $\mathbf{IV_d}$–**6LU7** interactions shown by the active-site amino acids in each trajectory frame (white denotes zero interaction, while a deep color indicates more interactions).

occurred with Met49; both interactions occurred for 55% of the simulation time. Fig. 11 shows the ligand–protein alignment for the simulation times.

To monitor the $\mathbf{IV_d}$–protein interactions during the simulations, a plot of the active-site residues was plotted against trajectory frames (Fig. 12). Notably, Glu166 formed the strongest interaction while His41, Met49, and Ser144 were in contact with $\mathbf{IV_d}$ most of the time. However, Asn142 and Gly144 formed an interaction from time to time, while His163 formed a contact only after 40 ns of simulation time.

2.5. MM-GBSA study

The average MM-GBSA binding energy was generated using the thermal_mmgbsa.py python script provided by Schrodinger, which also generated the Coulomb energy, covalent binding energy, van der Waals energy, lipophilic energy, generalized Born electrostatic solvation energy, and hydrogen-bonding energy (see Table 4 for all the obtained data).

From the MM-GBSA calculations, the most favored binding energy was exhibited by $\mathbf{IV_d}$ (−54.98 kcal mol^{-1}), and $\mathbf{IV_d}$ also exhibited a strong lipophilic energy, pi–pi interaction, and van der Waals energy.

3. Conclusion

A new series of 1,3,4-oxadiazoles carrying the isatin moiety ($\mathbf{IV_{a–g}}$) were designed as potential SARS-CoV-2 M^{pro} inhibitors and compared with both the reported isatin derivative with a

promising SARS-CoV-2 M^{pro} inhibitory activity ($\mathbf{I_a}$), and the co-crystallized inhibitor (**N3**) as reference standards. Consistent with the design rationale, molecular docking studies revealed the promising binding modes and affinities of all the newly designed compounds within the SARS-COV-2 M^{pro} active site compared to the reported lead compound ($\mathbf{I_a}$). Furthermore, molecular dynamics simulations showed that most ligand–protein complexes were stable during the simulations, and most ligands showed tight binding to the protein active site (RMSD $<$ 10 Å). MD simulations also showed that Glu166 was a critical residue for ligand stability. The obtained MM-GBSA data promoted among others, $\mathbf{IV_d}$, with a binding energy of -54.98 kcal mol^{-1}. On the other hand, antiviral activity evaluation showed that compounds $\mathbf{IV_e}$ and $\mathbf{IV_g}$ exhibited higher activities than **N3** against SARS-CoV-2 in Vero-E6 cells (IC_{50} values of 13.84 μM and 4.63 μM and selectivity indices of 4.1 and 5.9, respectively). According to the antiviral activity assay results, it was decided to further assay compound $\mathbf{IV_g}$ for enzyme inhibition activity against SARS-CoV-2 M^{pro}. Unexpectedly, compound $\mathbf{IV_g}$ was found to demonstrate an IC_{50} of 16.60 μM against SARS-CoV-2 M^{pro}, which was considered as moderate activity compared with the reported potent SARS-CoV-2 M^{pro} inhibitor **N3** (IC_{50} = 0.40 μM). The high selective antiviral activity of $\mathbf{IV_g}$ in the cell protection assay, regardless of its reduced M^{pro} inhibitory effect, suggested $\mathbf{IV_g}$ as a lead compound that needs further optimization for better binding to the enzyme and better cellular activity to attain broad-spectrum anti-SARS-CoV-2 agents. Thus, the significance of this manuscript comes in repurposing this class of compounds as anti-SARS-CoV-2 agents and the obtained results may shed light on the structure–activity relationship required for SARS-CoV-2 inhibition, to eventually help in the future introduction of newly synthesized drug candidates that target SARS-CoV-2.

4. Experimental

4.1. Chemistry

4.1.1. General. Unless specified, all chemicals were of commercial grade, were used without further purification, and were obtained from Aldrich Chemical Co. (Milwaukee, WI, USA). Melting points were obtained using Stuart melting point apparatus and were uncorrected. Microanalyses for C, H, and N were performed at the Regional Center for Mycology and Biotechnology, Al-Azhar University. IR spectra were recorded from potassium bromide discs using a Shimadzu IR 435 spectrophotometer (Shimadzu Corp., Kyoto, Japan) at the Faculty of Pharmacy, Cairo University, Cairo, Egypt, and are expressed in wavenumbers (cm^{-1}). ^{1}H NMR spectra were recorded using a Bruker 400 MHz (Bruker Corp., Billerica, MA, USA) spectrophotometer at the Faculty of Pharmacy, Cairo University, Cairo, Egypt. Dimethyl sulfoxide (DMSO) was used as a solvent, and chemical shifts were recorded in ppm on the δ scale and coupling constants (J) are reported in Hz. The exchangeable protons were exchanged using D_2O. ^{13}C NMR spectra were recorded using a Bruker 100 MHz spectrophotometer at the Faculty of Pharmacy, Cairo University, Cairo, Egypt. The progress of the reactions was monitored *via* TLC using MERCK pre-coated aluminum sheet plates coated with silica gel 60F 254. The developing solvents were ethyl acetate/hexane (7 : 3), and the spots were visualized at 366, 254 nm using UV Vilber Lourmat 77202 equipment (Vilber, Marne La Vallee, France).[51]

4.1.2. General procedure for the preparation of (*E*)-5-substituted-3-{[5-(4-substituted phenyl)-1,3,4-oxadiazol-2-yl]imino}indolin-2-one derivatives ($\mathbf{IV_{a–g}}$). A mixture of equimolar amounts (10 mmol) of oxadiazole derivatives $\mathbf{II_{a–c}}$ and isatin derivatives $\mathbf{III_{a–c}}$ were dissolved in acetic acid (30 mL) and refluxed for 38–50 hours. The reaction mixture was then allowed to cool. The formed crystals were filtered, washed with water, dried, and crystallized from aqueous ethanol.

(E)-3-{[5-Phenyl-1,3,4-oxadiazol-2-yl]imino}indolin-2-one ($\mathbf{IV_a}$). Orange crystals (0.81 g, 28%), m.p. 282–284 °C; IR (KBr, ν_{max} cm^{-1}): 3236 (NH of isatin), 1693 (C=O). ^{1}H NMR (DMSO-d_6, 400 MHz) δ: 6.97 (d, 1H, J = 7.80 Hz, Ar–H), 7.13 (dd, 1H, J = 7.56 Hz, Ar–H), 7.41 (dd, 1H, J = 7.70 Hz, Ar–H), 7.63 (dd, 3H, J = 7.52 Hz, Ar–H), 7.69 (d, 1H, J = 7.16 Hz, Ar–H), 7.90 (d, 2H, J = 7.72 Hz, Ar–H), 11.38 (s, 1H, NH, D_2O exchangeable), 13.94 (s, 1H, OH, D_2O exchangeable). ^{13}C NMR (DMSO-d_6, 100 MHz) δ: 111.71, 120.29, 121.44, 123.24, 127.88, 129.64, 132.29, 132.55, 133.33, 142.94, 163.53. Anal. calcd for $C_{16}H_{10}N_4O_2$ (290.28): C, 66.20; H, 3.47; N, 19.30; O, 11.02; found: C, 66.43; H, 3.65; N, 19.58.

(E)-3-{[5-(4-Chlorophenyl)-1,3,4-oxadiazol-2-yl]imino}indolin-2-one ($\mathbf{IV_b}$). Brown crystals (1.40 g, 43%), m.p. 276–278 °C; IR (KBr, ν_{max} cm^{-1}): 3217 (NH of isatin), 1670 (C=O). ^{1}H NMR (DMSO-d_6, 400 MHz) δ: 6.97 (d, 1H, J = 7.40 Hz, Ar–H), 7.13 (dd, 1H, J = 7.36 Hz, Ar–H), 7.42 (dd, 1H, J = 7.24 Hz, Ar–H), 7.60 (d, 1H, J = 6.12 Hz, Ar–H), 7.70 (d, 2H, J = 7.76 Hz, Ar–H), 7.91 (d, 2H, J = 8.00 Hz, Ar–H), 11.39 (s, 1H, NH, D_2O exchangeable), 13.91 (s, 1H, OH, D_2O exchangeable). ^{13}C NMR (DMSO-d_6, 100 MHz) δ: 111.73, 120.19, 121.50, 123.25, 129.73, 131.31, 132.39, 138.15, 143.00, 163.48. Anal. calcd for $C_{16}H_9ClN_4O_2$ (324.72): C, 59.18; H, 2.79; Cl, 10.92; N, 17.25; O, 9.85; found: C, 59.42; H, 2.95; N, 17.12. EIMS, m/z: 324.16, 75.00 (100%).

(E)-3-{[5-(4-Methoxyphenyl)-1,3,4-oxadiazol-2-yl]imino}indolin-2-one ($\mathbf{IV_c}$). Brown crystals (1.22 g, 38%), m.p. 285–287 °C; IR (KBr, ν_{max} cm^{-1}): 3169 (NH of isatin), 1671 (C=O). ^{1}H NMR (DMSO-d_6, 400 MHz) δ: 3.87 (s, 3H, OCH_3), 6.96–7.89 (m, 8H, Ar–H), 11.37 (s, 1H, NH, D_2O exchangeable), 13.90 (s, 1H, OH, D_2O exchangeable). ^{13}C NMR (DMSO-d_6, 100 MHz) δ: 56.06, 111.67, 114.94, 120.38, 121.30, 123.18, 124.53, 129.96, 132.07, 137.99, 142.77, 163.32. Anal. calcd for $C_{17}H_{12}N_4O_3$ (320.30): C, 63.75; H, 3.78; N, 17.49; O, 14.99; found: C, 63.98; H, 3.94; N, 17.62.

(E)-5-Chloro-3-{[5-(4-chlorophenyl)-1,3,4-oxadiazol-2-yl]imino}-indolin-2-one ($\mathbf{IV_d}$). Yellowish orange crystals (0.72 g, 20%), m.p. $>$ 300 °C; IR (KBr, ν_{max} cm^{-1}): 3228 (NH of isatin), 1682 (C=O). ^{1}H NMR (DMSO-d_6, 400 MHz) δ: 6.97 (d, 1H, J = 10.00 Hz, Ar–H),

7.43 (d, 1H, J = 10.00 Hz, Ar–H), 7.58 (s, 1H, Ar–H), 7.69 (d, 2H, J = 6.8 Hz, Ar–H), 7.90 (d, 2H, J = 8.00 Hz, Ar–H), 11.49 (s, 1H, NH, D_2O exchangeable), 13.82 (s, 1H, OH, D_2O exchangeable). ^{13}C NMR (DMSO-d_6, 100 MHz) δ: 113.29, 121.00, 122.09, 127.40, 129.78, 130.05, 131.14, 131.79, 133.10, 138.37, 141.68, 163.29. Anal. calcd for $C_{16}H_8Cl_2N4O_2$ (359.17): C, 53.50; H, 2.25; Cl, 19.74; N, 15.60; O, 8.91; found: C, 53.67; H, 2.42; N, 15.76. EIMS, m/z: 359.66, 75.03 (100%).

*(E)-5-Bromo-3-{[5-phenyl-1,3,4-oxadiazol-2-yl]imino}indolin-2-one (**IV$_e$**).* Orange brown crystals (0.63 g, 17%), m.p. 281–283 °C; IR (KBr, ν_{max} cm^{-1}): 3251 (NH of isatin), 1678 (C=O). ^{1}H NMR (DMSO-d_6, 400 MHz) δ: 6.93 (d, 1H, J = 8.32 Hz, Ar–H), 7.56 (d, 1H, J = 8.36 Hz, Ar–H), 7.63 (dd, 2H, J = 7.72 Hz, Ar–H), 7.70 (dd, 1H, Ar–H), 7.712 (s, 1H, Ar–H), 7.90 (d, 2H, J = 7.16 Hz, Ar–H), 11.50 (s, 1H, NH, D_2O exchangeable), 13.87 (s, 1H, OH, D_2O exchangeable). ^{13}C NMR (DMSO-d_6, 100 MHz) δ: 113.72, 114.91, 122.43, 123.64, 127.99, 129.67, 132.35, 133.46, 134.45, 142.08, 163.23. Anal. calcd for $C_{16}H_9BrN_4O_2$ (369.17): C, 52.05; H, 2.46; Br, 21.64; N, 15.18; O, 8.67; found: C, 52.19; H, 2.70; N, 14.97. EIMS, m/z: 369.57, 75.04 (100%).

*(E)-5-Bromo-3-{[5-(4-chlorophenyl)-1,3,4-oxadiazol-2-yl]imino}-indolin-2-one (**IV$_f$**).* Orange crystals (0.93 g, 23%), m.p. > 300 °C; IR (KBr, ν_{max} cm^{-1}): 3238 (NH of isatin), 1675 (C=O). ^{1}H NMR (DMSO-d_6, 400 MHz) δ: 6.93 (d, 1H, J = 6.40 Hz, Ar–H), 7.57 (d, 1H, J = 10.40 Hz, Ar–H), 7.70 (s, 1H, Ar–H), 7.69 (d, 2H, J = 8.80, Ar–H), 7.90 (d, 2H, J = 8.80 Hz, Ar–H), 11.53 (s, 1H, NH, D_2O exchangeable), 13.80 (s, 1H, OH, D_2O exchangeable). ^{13}C NMR (DMSO-d_6, 100 MHz) δ: 113.73, 114.97, 122.33, 123.72, 129.77, 131.12, 134.58, 142.05, 163.13. Anal. calcd for $C_{16}H_8BrClN_4O_2$ (403.62): C, 47.61; H, 2.00; Br, 19.80; Cl, 8.78; N, 13.88; O, 7.93; found: C, 47.89; H, 2.13; N, 14.12. EIMS, m/z: 403.35, 75.03 (100%).

*(E)-5-Bromo-3-{[5-(4-methoxyphenyl)-1,3,4-oxadiazol-2-yl]imino}-indolin-2-one (**IV$_g$**).* Yellowish brown crystals (1.27 g, 32%), m.p. 295–297 °C; IR (KBr, ν_{max} cm^{-1}): 3219 (NH of isatin), 1674 (C=O). ^{1}H NMR (DMSO-d_6, 400 MHz) δ: 3.87 (s, 3H, OCH_3), 6.93 (d, 1H, J = 8.32 Hz, Ar–H), 7.15 (d, 2H, J = 8.80 Hz, Ar–H), 7.55 (d, 1H, J = 8.28 Hz, Ar–H), 7.70 (s, 1H, Ar–H), 7.87 (d, 2H, J = 8.80 Hz, Ar–H), 11.49 (s, 1H, NH, D_2O exchangeable), 13.83 (s, 1H, OH, D_2O exchangeable). ^{13}C NMR (DMSO-d_6, 100 MHz) δ: 56.09, 113.34, 113.66, 114.91, 114.99, 122.52, 123.53, 124.33, 130.10, 134.25, 141.81, 163.23. Anal. calcd for $C_{17}H_{11}BrN_4O_3$ (399.20): C, 51.15; H, 2.78; Br, 20.02; N, 14.03; O, 12.02; found: C, 50.96; H, 3.02; N, 14.29. EIMS, m/z: 399.30, 77.19 (100%).

4.2. Biological evaluations

4.2.1. MTT cytotoxicity assay. The MTT assay was used to estimate the minimum concentrations of the synthesized compounds that can induce 50% toxicity (CC_{50}) in the cells used. In the beginning, ddH_2O with 10% DMSO was used to dissolve the synthesized compounds, which were diluted during work with Dulbecco's Modified Eagle's Medium (DMEM). Herein, the MTT method with small modifications was carried out utilizing Vero-E6 cells, which are appropriate for the virus propagation. Thus, to be cultivated, the Vero-E6 cells were kept in 96-well plates at 37 °C in 5% CO_2 for 24 h. The synthesized compounds were diluted with DMEM in HA plates in triplicate and then flowed onto the prepared cells after irrigating twice using sterile phosphate buffer saline (PBS). 24 h later, following removal of the supernatant, the cell monolayers were rinsed three times with sterile PBS. Subsequently, MTT solution was added to each well (20 ml of 5 mg ml^{-1} stock solution) before incubation at 37 °C for 4 h. Thus, acidified isopropanol (200 ml) was used to dissolve the formed formazan crystals. The solution absorbance was measured using a multi-well plate reader (λ_{max} = 540 nm) against a reference wavelength (λ_{max} = 620 nm).[53,54] Finally, the cytotoxicity % of the synthesized compounds was calculated compared with the control cells (untreated cells) as follows:

$$\%\ \text{cytotoxicity} = \frac{(\text{the absorbance of cells without treatment} - \text{absorbance of cells with treatment}) \times 100}{\text{the absorbance of cells without treatment}}.$$

4.2.2. Half-maximal inhibitory concentration (IC_{50}) determination. 96-well tissue culture plates were used for incubating the Vero-E6 cells (2.4×10^4) overnight at 37 °C in a 5% CO_2 atmosphere. The cell monolayers were washed with PBS solution only once. The cell monolayers were then treated with various serial dilutions of the synthesized compounds together with a fixed dilution from the virus (*h*CoV-19/Egypt/NRC-03/2020 (Accession Number on GSAID: EPI_ISL_430820)) following the TCID50 test. Before starting incubation, they were kept at RT for 1 h. Besides, the cell monolayers were treated with DMEM (100 ml) at different concentrations of the test samples and virus, then left in 5% CO_2 for 72 h at 37 °C. Thereafter, cell fixation was performed using 4% paraformaldehyde (100 ml) for 2 h followed by the staining step using 0.1% crystal violet in distilled H_2O (50 ml) at RT for 15 min. Then, the crystal violet dye per well was dissolved using absolute CH_3OH (100 ml) to measure the optical density of the produced color using an Anthos Zenyth 200rt plate reader at 570 nm.[55]

4.2.3. SARS-CoV-2 main protease inhibitory activity. Recombinant SARS-CoV-2 M^{pro} was expressed in *Escherichia coli* and subsequently purified. To characterize the enzymatic activity of SARS-CoV-2 M^{pro} for compound **IV$_g$** with the highest anti-SARS-CoV-2 inhibitory activity, a fluorescence resonance energy transfer assay was applied.[56] Briefly, the activity of SARS-CoV-2 M^{pro} was measured using a continuous kinetic assay, with the fluorescently-labeled peptide substrate MCA-AVLQSGFR-Lys(Dnp)-Lys-NH2 (GL Biochem, Shanghai), using wavelengths of 320 nm and 405 nm for excitation and emission, respectively. The protease activity was monitored as a time-course measurement of the increase in the fluorescence signal after incubation with serial dilution of the inhibitor **IV$_g$**. The compound was tested in 10-dose IC_{50} mode with a 3-fold serial dilution starting at 100 μM.

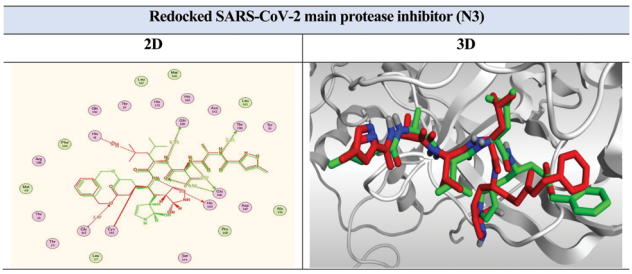

Fig. 13 2D and 3D representations for the docked co-crystallized inhibitor **N3** inside the SARS-CoV-2 main protease active site. (The original **N3** inhibitor is represented in green while the docked one is represented in red.)

4.3. Docking studies

A molecular docking study of the designed oxoindole–oxadiazole hybrids $\mathbf{IV_{a-g}}$ at the SARS-CoV-2 M^{pro} active site was performed using MOE 2019.0102 drug-design software[57] to evaluate the activity of the newly synthesized oxadiazoles compared with both the previously reported isatin derivative ($\mathbf{I_a}$), which has a promising SARS-CoV-2 M^{pro} inhibitory activity,[26] and **N3**, a potent SARS-CoV-2 M^{pro} inhibitor.[56] The Protein Data Bank (http://www.rcsb.org/, PDB code 6LU7, resolution of 2.16 Å)[56] was used to obtain the X-ray structure of the target SARS-CoV-2 M^{pro}–**N3** complex, which was prepared for docking studies using the previously described default method.[40,46]

At first, a validation process was performed for the docking protocol by redocking of the co-crystallized inhibitor, **N3** (Fig. 13), and the obtained low RMSD value indicated the valid performance (RMSD = 1.46 Å).[58,59]

The applied docking methodology involved opening the prepared receptor pocket in the MOE window, and the process type was chosen for general docking.[60–62] The Site Finder was used to select the same active site of the **N3** inhibitor using dummy atoms.[63,64] The applied forcefield was Amber10:EHT. The scoring methodology was selected as GBVI/WSA dG for the refinement methodology, which was selected as a rigid receptor.[65,66] On the other hand, the scoring methodology was applied as London dG for the placement methodology, which was selected as a triangle matcher.[67,68] The prepared MDB file containing the newly synthesized derivatives ($\mathbf{IV_{a-g}}$) together with the previously reported isatin derivative ($\mathbf{I_a}$)[26] and (**N3**) inhibitor[56] was inserted and then the docking calculations were performed automatically to obtain poses with the most acceptable binding scores, rmsd_refine values, and interaction modes.[69,70]

4.4. Molecular dynamics simulations

The molecular dynamics simulations were performed using the Desmond simulation package of Schrödinger LLC.[71] The *NPT* ensemble at a temperature of 300 K and a pressure 1 bar was applied in all runs. The simulation length was 100 ns with a relaxation time of 1 ps for all selected ligands. The entire methodology was applied as previously described in detail.[72]

The complete ligand–protein interactions were analyzed using the simulation interaction diagram tool in the Desmond MD package. The stability of MD simulations was monitored by looking at the RMSD of the ligand and protein atom positions with time.

4.5. MD trajectory analysis and prime MM-GBSA calculations

The Maestro software simulation interactions diagram panel was used to observe influence of the interactions on the ligand–protein stability. Generally, molecular mechanics-generalized Born solvent accessibility (MM-GBSA) calculations were carried out to estimate the ligand strain energies and the ligand binding free energies for docked molecules over the 100 ns period using the thermal_mmgbsa.py python script delivered *via* Schrödinger. The average binding energy was calculated as previously described.[72]

Conflicts of interest

The authors declare no conflict of interest.

References

1 W. Dai, *et al.*, Structure-based design of antiviral drug candidates targeting the SARS-CoV-2 main protease, *Science*, 2020, **368**(6497), 1331–1335.
2 A. A. Al-Karmalawy, *et al.*, Coronavirus Disease (COVID-19) Control between Drug Repurposing and Vaccination: A Comprehensive Overview, *Vaccines*, 2021, **9**(11), 1317.
3 H. Tian, *et al.*, An investigation of transmission control measures during the first 50 days of the COVID-19 epidemic in China, *Science*, 2020, **368**(6491), 638–642.
4 A. Abo Elmaaty, *et al.*, Computational Insights on the Potential of Some NSAIDs for Treating COVID-19: Priority Set and Lead Optimization, *Molecules*, 2021, **26**(12), 3772.
5 A. E. Abdallah, *et al.*, Design and synthesis of new 4-(2-nitrophenoxy)benzamide derivatives as potential antiviral agents: molecular modeling and in vitro antiviral screening, *New J. Chem.*, 2021, **45**, 16557–16571.
6 E. G. Alexander, *et al.*, The species and its viruses–a statement of the Coronavirus Study Group, *Biorxiv Cold Spring Harb Lab*, 2020, 1–15.
7 W. Director, General's opening remarks at the media briefing on COVID-19-11 March 2020. Erişim: https://www.who.int/dg/speeches/detail/who-director-general-sopening-remarks-at-the-media-briefing-on-covid-19-11-march-2020, 2020.
8 A. A. Sarhan, N. A. Ashour and A. A. Al-Karmalawy, The journey of antimalarial drugs against SARS-CoV-2: Review article, *Inform. Med. Unlocked*, 2021, 100604.
9 A. Albini, *et al.*, The SARS-CoV-2 receptor, ACE-2, is expressed on many different cell types: implications for ACE-inhibitor-and angiotensin II receptor blocker-based cardiovascular therapies, *Intern. Emerg. Med.*, 2020, **15**, 759–766.

10 M. Mei and X. Tan, Current Strategies of Antiviral Drug Discovery for COVID-19, *Front. Mol. Biosci.*, 2021, **8**(310), 671263.
11 R. Hilgenfeld, From SARS to MERS: crystallographic studies on coronaviral proteases enable antiviral drug design, *FEBS J.*, 2014, **281**(18), 4085–4096.
12 V. N. Badavath, *et al.*, Determination of potential inhibitors based on isatin derivatives against SARS-CoV-2 main protease (mpro): a molecular docking, molecular dynamics and structure-activity relationship studies, *J. Biomol. Struct. Dyn.*, 2020, 1–19.
13 K. Anand, *et al.*, Coronavirus main proteinase (3CLpro) structure: basis for design of anti-SARS drugs, *Science*, 2003, **300**(5626), 1763–1767.
14 A. Voss, *et al.*, Publishing in face of the COVID-19 pandemic, *Int. J. Antimicrob. Agents*, 2020, **56**(1), 106081.
15 K. Y. Wang, *et al.*, Structure of Mpro from COVID-19 virus and discovery of its inhibitors, *Nature*, 2020, **582**, 289–293.
16 A. A. Al-Karmalawy, *et al.*, Molecular Docking and Dynamics Simulation Revealed the Potential Inhibitory Activity of ACEIs Against SARS-CoV-2 Targeting the hACE2 Receptor, *Front. Chem.*, 2021, **9**(227), 661230.
17 A. A. Al-Karmalawy and I. H. J. P. S. Eissa, Molecular docking and dynamics simulations reveal the potential of anti-HCV drugs to inhibit COVID-19 main protease, *Pharm. Sci.*, 2021, **27**(1), S109–S121.
18 R. Alnajjar, *et al.*, Molecular docking, molecular dynamics, and in vitro studies reveal the potential of angiotensin II receptor blockers to inhibit the COVID-19 main protease, *Heliyon*, 2020, **6**(12), e05641.
19 A. A. Elmaaty, *et al.*, Revisiting activity of some glucocorticoids as a potential inhibitor of SARS-CoV-2 main protease: theoretical study, *RSC Adv.*, 2021, **11**(17), 10027–10042.
20 L. Zhang, *et al.*, Crystal structure of SARS-CoV-2 main protease provides a basis for design of improved α-ketoamide inhibitors, *Science*, 2020, **368**(6489), 409–412.
21 R. Soltane, *et al.*, Strong Inhibitory Activity and Action Modes of Synthetic Maslinic Acid Derivative on Highly Pathogenic Coronaviruses: COVID-19 Drug Candidate, *Pathogens*, 2021, **10**(5), 623.
22 H. Liu, *et al.*, Scutellaria baicalensis extract and baicalein inhibit replication of SARS-CoV-2 and its 3C-like protease in vitro, *J. Enzyme Inhib. Med. Chem.*, 2021, **36**(1), 497–503.
23 A. A. Elmaaty, *et al.*, In a search for potential drug candidates for combating COVID-19: computational study revealed salvianolic acid B as a potential therapeutic targeting 3CLpro and spike proteins, *J. Biomol. Struct. Dyn.*, 2021, 1–28.
24 A. A. Zaki, *et al.*, Molecular docking reveals the potential of Cleome amblyocarpa isolated compounds to inhibit COVID-19 virus main protease, *New J. Chem.*, 2020, **44**(39), 16752–16758.
25 A. A. Zaki, *et al.*, Calendulaglycoside A Showing Potential Activity Against SARS-CoV-2 Main Protease: Molecular Docking, Molecular Dynamics, and SAR Studies, *J. Tradit. Complement. Med.*, 2021, DOI: 10.1016/j.jtcme.2021.05.001, https://www.sciencedirect.com/science/article/pii/S2225411021000559.
26 P. Liu, *et al.*, Potent inhibitors of SARS-CoV-2 3C-like protease derived from N-substituted isatin compounds, *Eur. J. Med. Chem.*, 2020, **206**, 112702.
27 M. A. Soltan, *et al.*, Proteome Based Approach Defines Candidates for Designing a Multitope Vaccine against the Nipah Virus, *Int. J. Mol. Sci.*, 2021, **22**(17), 9330.
28 M. A. Soltan, *et al.*, In Silico Prediction of a Multitope Vaccine against Moraxella catarrhalis: Reverse Vaccinology and Immunoinformatics, *Vaccines*, 2021, **9**(6), 669.
29 A. A. Al-Karmalawy, *et al.*, Naturally Available Flavonoid Aglycones as Potential Antiviral Drug Candidates against SARS-CoV-2, *Molecules*, 2021, **26**(21), 6559.
30 H. A. El Gizawy, *et al.*, Pimenta dioica (L.) Merr. Bioactive Constituents Exert Anti-SARS-CoV-2 and Anti-Inflammatory Activities: Molecular Docking and Dynamics, In Vitro, and In Vivo Studies, *Molecules*, 2021, **26**(19), 5844.
31 A. El-Demerdash, *et al.*, Investigating the structure–activity relationship of marine natural polyketides as promising SARS-CoV-2 main protease inhibitors, *RSC Adv.*, 2021, **11**(50), 31339–31363.
32 D. Elebeedy, *et al.*, Anti-SARS-CoV-2 activities of tanshinone IIA, carnosic acid, rosmarinic acid, salvianolic acid, baicalein, and glycyrrhetinic acid between computational and in vitro insights, *RSC Adv.*, 2021, **11**(47), 29267–29286.
33 M. I. A. Hamed, *et al.*, β-Blockers bearing hydroxyethylamine and hydroxyethylene as potential SARS-CoV-2 Mpro inhibitors: rational based design, in silico, in vitro, and SAR studies for lead optimization, *RSC Adv.*, 2021, **11**(56), 35536–35558.
34 A. Kandeil, *et al.*, Bioactive Polyphenolic Compounds Showing Strong Antiviral Activities against Severe Acute Respiratory Syndrome Coronavirus 2, *Pathogens*, 2021, **10**(6), 758.
35 A. Mahmoud, *et al.*, Telaprevir is a potential drug for repurposing against SARS-CoV-2: computational and *in vitro* studies, *Heliyon*, 2021, **7**(9), DOI: 10.1016/j.heliyon.2021.e07962.
36 D. B. Mahmoud, *et al.*, Delineating a potent antiviral activity of Cuphea ignea extract loaded nano-formulation against SARS-CoV-2: In silico and in vitro studies, *J. Drug Delivery Sci. Technol.*, 2021, 102845.
37 M. M. Shehata, *et al.*, In Silico and In Vivo Evaluation of SARS-CoV-2 Predicted Epitopes-Based Candidate Vaccine, *Molecules*, 2021, **26**(20), 6182.
38 D. Elebeedy, *et al.*, In vitro and computational insights revealing the potential inhibitory effect of Tanshinone IIA against influenza A virus, *Comput. Biol. Med.*, 2021, 105149.
39 M. S. Alesawy, *et al.*, Design and discovery of new 1, 2, 4-triazolo [4, 3-c] quinazolines as potential DNA intercalators and topoisomerase II inhibitors, *Arch. Pharm.*, 2020, e2000237.
40 A. A. Al-Karmalawy and M.J.N.J.o.C. Khattab, Molecular modelling of mebendazole polymorphs as a potential colchicine binding site inhibitor, *New J. Chem.*, 2020, **44**(33), 13990–13996.

41 R. T. Diab, *et al.*, Design and Synthesis of a New Series of 3,5-Disubstituted-1,2,4-Oxadiazoles as Potential Colchicine Binding Site Inhibitors: Antiproliferative activity, Molecular docking, and SAR Studies, *New J. Chem.*, 2021, **45**, 21657–21669.
42 M. A. Aziz, *et al.*, Design, Synthesis, Biological Evaluation, 2D-QSAR Modeling, and Molecular Docking Studies of Novel 1H-3-Indolyl Derivatives as Significant Antioxidants, *Int. J. Mol. Sci.*, 2021, **22**(19), 10396.
43 S. G. Elia, *et al.*, Loperamide potentiates doxorubicin sensitivity in triple-negative breast cancer cells by targeting MDR1 and JNK and suppressing mTOR and Bcl-2: In vitro and molecular docking study, *J. Biochem. Mol. Toxicol.*, 2021, e22938.
44 M. F. Elshal, Concanavalin-A shows synergistic cytotoxicity with tamoxifen via inducing apoptosis in estrogen receptor-positive breast cancer, *Pharm. Sci.*, 2022, **28**(1), 76–85.
45 M. H. El-Shershaby, *et al.*, The antimicrobial potential and pharmacokinetic profiles of novel quinoline-based scaffolds: synthesis and in silico mechanistic studies as dual DNA gyrase and DHFR inhibitors, *New J. Chem.*, 2021, **45**, 13986–14004.
46 M. Khattab and A. A. Al-Karmalawy, Revisiting Activity of Some Nocodazole Analogues as a Potential Anticancer Drugs Using Molecular Docking and DFT Calculations, *Front. Chem.*, 2021, **9**, 92.
47 A. G. A. El-Helby, *et al.*, Design, synthesis, molecular docking, and anticancer activity of benzoxazole derivatives as VEGFR-2 inhibitors, *Arch. Pharm.*, 2019, **352**(10), 1900113.
48 A. G. A. El-Helby, *et al.*, Benzoxazole/benzothiazole-derived VEGFR-2 inhibitors: Design, synthesis, molecular docking, and anticancer evaluations, *Arch. Pharm.*, 2019, **352**(12), 1900178.
49 M. M. Khalifa, *et al.*, Topo II inhibition and DNA intercalation by new phthalazine-based derivatives as potent anticancer agents: design, synthesis, anti-proliferative, docking, and in vivo studies, *J. Enzyme Inhib. Med. Chem.*, 2022, **37**(1), 299–314.
50 J. M. Parks and J. C. Smith, How to discover antiviral drugs quickly, *N. Engl. J. Med.*, 2020, **382**(23), 2261–2264.
51 V. Gupta, *et al.*, Synthesis and antimicrobial activity of some new 3–[5-(4-substituted) phenyl-1, 3, 4-oxadiazole-2yl]-2-styrylquinazoline-4 (3H)-ones, *Med. Chem. Res.*, 2008, **17**(2), 205–211.
52 G. Li and E. De Clercq, Therapeutic options for the 2019 novel coronavirus (2019-nCoV), *Nat. Rev. Drug Discovery*, 2020, **19**, 149–150. PMID.
53 M. W. Al-Rabia, *et al.*, Repurposing of Sitagliptin-Melittin Optimized Nanoformula against SARS-CoV-2: Antiviral Screening and Molecular Docking Studies, *Pharmaceutics*, 2021, **13**(3), 307.
54 M. Feoktistova, P. Geserick and M. Leverkus, Crystal violet assay for determining viability of cultured cells, *Cold Spring Harb. Protoc.*, 2016, **2016**(4), prot087379.
55 N. P. Marques, *et al.*, A preliminary comparison between the effects of red and infrared laser irradiation on viability and proliferation of SHED, *Lasers Med. Sci.*, 2019, **34**(3), 465–471.
56 Z. Jin, *et al.*, Structure of M pro from SARS-CoV-2 and discovery of its inhibitors, *Nature*, 2020, **582**(7811), 289–293.
57 C. C. G. Inc, *Molecular operating environment (MOE)* 2016, Chemical Computing Group Inc 1010 Sherbooke St. West, Suite# 910, Montreal.
58 I. W. Davis and D. Baker, RosettaLigand docking with full ligand and receptor flexibility, *J. Mol. Biol.*, 2009, **385**(2), 381–392.
59 S. G. Eliaa, *et al.*, Empagliflozin and Doxorubicin Synergistically Inhibit the Survival of Triple-Negative Breast Cancer Cells via Interfering with the mTOR Pathway and Inhibition of Calmodulin: In Vitro and Molecular Docking Studies, *ACS Pharmacol. Transl. Sci.*, 2020, **3**(6), 1330–1338.
60 A. Ghanem, *et al.*, Tanshinone IIA synergistically enhances the antitumor activity of doxorubicin by interfering with the PI3K/AKT/mTOR pathway and inhibition of topoisomerase II: in vitro and molecular docking studies, *New J. Chem.*, 2020, **44**(40), 17374–17381.
61 R. M. Samra, *et al.*, Bioassay-guided isolation of a new cytotoxic ceramide from Cyperus rotundus L, *S. Afr. J. Bot.*, 2021, **139**, 210–216.
62 R. M. Hazem, *et al.*, Pirfenidone and vitamin D mitigate renal fibrosis induced by doxorubicin in mice with Ehrlich solid tumor, *Life Sci.*, 2021, 120185.
63 A. A. Zaki, *et al.*, Isolation of cytotoxic active compounds from Reichardia tingitana with investigation of apoptosis mechanistic induction: In silico, in vitro, and SAR studies, *S. Afr. J. Bot.*, 2022, **144**, 115–123.
64 R. F. Taher, *et al.*, Two new flavonoids and anticancer activity of Hymenosporum flavum: in vitro and molecular docking studies, *J. HerbMed Pharmacol.*, 2021, **10**, 4.
65 T. Shoala, *et al.*, Nanobiotechnological Approaches to Enhance Potato Resistance against Potato Leafroll Virus (PLRV) Using Glycyrrhizic Acid Ammonium Salt and Salicylic Acid Nanoparticles, *Horticulturae*, 2021, **7**(10), 402.
66 M. A. Raslan, *et al.*, Cordyline fruticosa (L.) A. Chev. leaves: isolation, HPLC/MS profiling and evaluation of nephroprotective and hepatoprotective activities supported by molecular docking, *New J. Chem.*, 2021, **45**, 22216–22233.
67 M. Khattab and A. A. Al-Karmalawy, Computational repurposing of benzimidazole anthelmintic drugs as potential colchicine binding site inhibitors, *Future Med. Chem.*, 2021, **13**(19), DOI: 10.4155/fmc-2020-0273.
68 A. A. Gaber, *et al.*, Pharmacophore-linked pyrazolo[3,4-d]pyrimidines as EGFR-TK inhibitors: Synthesis, anticancer evaluation, pharmacokinetics, and in silico mechanistic studies, *Arch. Pharm.*, 2021, e2100258.
69 M. H. El-Shershaby, *et al.*, From triazolophthalazines to triazoloquinazolines: A bioisosterism-guided approach toward the identification of novel PCAF inhibitors with potential anticancer activity, *Bioorg. Med. Chem.*, 2021, **42**, 116266.
70 A. Al-Karmalawy, *et al.*, Design and Synthesis of New Quinoxaline Derivatives as Potential Histone Deacetylase

Inhibitors Targeting Hepatocellular Carcinoma: In Silico, In Vitro, and SAR Studies, *Front. Chem.*, 2021, 648.

71 S. Release, 3: Desmond molecular dynamics system, DE Shaw research, New York, NY, 2017. Maestro-Desmond Interoperability Tools, Schrödinger, New York, NY, 2017.

72 R. Alnajjar, N. Mohamed and N. Kawafi, Bicyclo [1.1. 1] Pentane as phenyl substituent in atorvastatin drug to improve physicochemical properties: drug-likeness, DFT, pharmacokinetics, docking, and molecular dynamic simulation, *J. Mol. Struct.*, 2021, **1230**, 129628.